

DIAGNOSTIC TECHNIQUES AND DEFECT CLASSIFICATION

G. Müller

University of Wuppertal

FB 8/ Physik, Gaußstr. 20, 5600 Wuppertal 1

Federal Republic of Germany

I. Introduction

During the last twelve years various diagnostic techniques have been used to clarify the origin of field limitations in superconducting cavities. These methods and the correlation between the specific experimental observations and known energy loss mechanisms are well described in the talk of H. Piel at the first workshop on RF superconductivity.¹ Most of them shall not be rediscussed here, since they have not been improved essentially in the meantime. Nevertheless, all of these methods have proven to be useful tools for the understanding of the phenomena, as for instance the detailed analysis of the RF signal, the detection of free electron currents inside the resonator by probes and measurements of the X-radiation or the light emitted from the cavity.

Since the development of systematic temperature mapping of the outer cavity wall immersed in a subcooled Helium bath at CERN in 1979 ² there has been a lot of progress in the achieved field levels especially of multicell accelerating structures. ³⁻⁵ This diagnostic technique has proven to be a reliable means of accurately locating sources of enhanced RF-losses within a Niobium resonator and allows therefore a guided removal of defects, which are known to be the prime causes for quenching. ⁶ The main advantage of temperature mapping with a rotating chain of carbon resistors in a subcooled He bath compared to other temperature measurements with fixed sensors or in a saturated He bath (for instance breakdown location by detection of second sound waves ⁷) consists in the enhanced sensitivity ⁸, which allows to determine the spatial distribution of RF-losses even for field levels far below quenching. As each energy loss mechanism will finally lead to an increased temperature of the cavity wall, principally all field and Q-limitations can be localized and identified. Therefore, this talk will be concentrated on the development of the temperature mapping technique and on what we have learned so far about defects.

In the first part I will discuss the dependence of the temperature mapping technique on different bath cooling conditions, on the thermal conductivity of the cavity wall and the rf frequency. The influence of these parameters on the spatial resolution and the present sensitivity limits are described. For the most interesting case of temperature mapping under subcooled He bath conditions the results of calibration measurements ^{9,10} are given, which correlate the measured temperature signals to the local heat flux on the cavity wall and which therefore allow the study of the energy loss mechanisms in a quantitative way. In the second part I will try to give a systematic characterization of localized defects which have caused quenching of superconducting Niobium cavities and which have been analyzed by the subsequent inspection of the cavity surface. This will give clues to the origin and suggestions for elimination of defects.

II. Temperature mapping technique

One of the main aims of a systematic temperature mapping is to determine the heat loss distribution in the cavity surface for different field levels to get a more detailed insight into the energy loss mechanism of a superconducting cavity. Unfortunately, we cannot measure the real interesting temperature distribution on the inner cavity surface. Any scanning resistor thermometer system will detect the temperature not only of the resonator wall but also of the surrounding liquid. For a quantitative determination of the locally dissipated power by the thermometer response therefore we have to consider the heat transport processes in the cavity wall and in the liquid Helium as well as the heat transfer coefficient at the metal-Helium interface. These are obviously influenced by the thermal conductivity and the thickness of the cavity wall and by the bath cooling conditions.

A useful means for investigation of the relative influence of the different parameters are model calculations¹¹⁻¹³, by which the thermal equilibrium situation over a metal-disc heated on one side by the electromagnetic field and cooled on the other side by liquid helium can be simulated. In Fig. 1 the result of such a calculation¹³ for a normal conducting pointlike defect (radius $r_D = 150 \mu\text{m}$, dissipated power $P_D = 40 \text{ mW}$) on a niobium wall of thickness $d = 2 \text{ mm}$ and of typical thermal conductivity (corresponding RRR = 40)¹⁴ is shown. Compared are the temperature profiles (axial) from the defect location to the helium bath for three different cooling conditions. Because of the same order of the heat transfer coefficients¹⁵ in nucleate boiling He I (at bath temperature $T_B = 2.5 \text{ K}$) and superfluid He II (at $T_B = 2.0 \text{ K}$) the corresponding temperature increase $\Delta T(z) = T(z) - T_B$ in the Niobium region look similar, resulting in an outer wall temperature increase of about 320mK. On the contrary

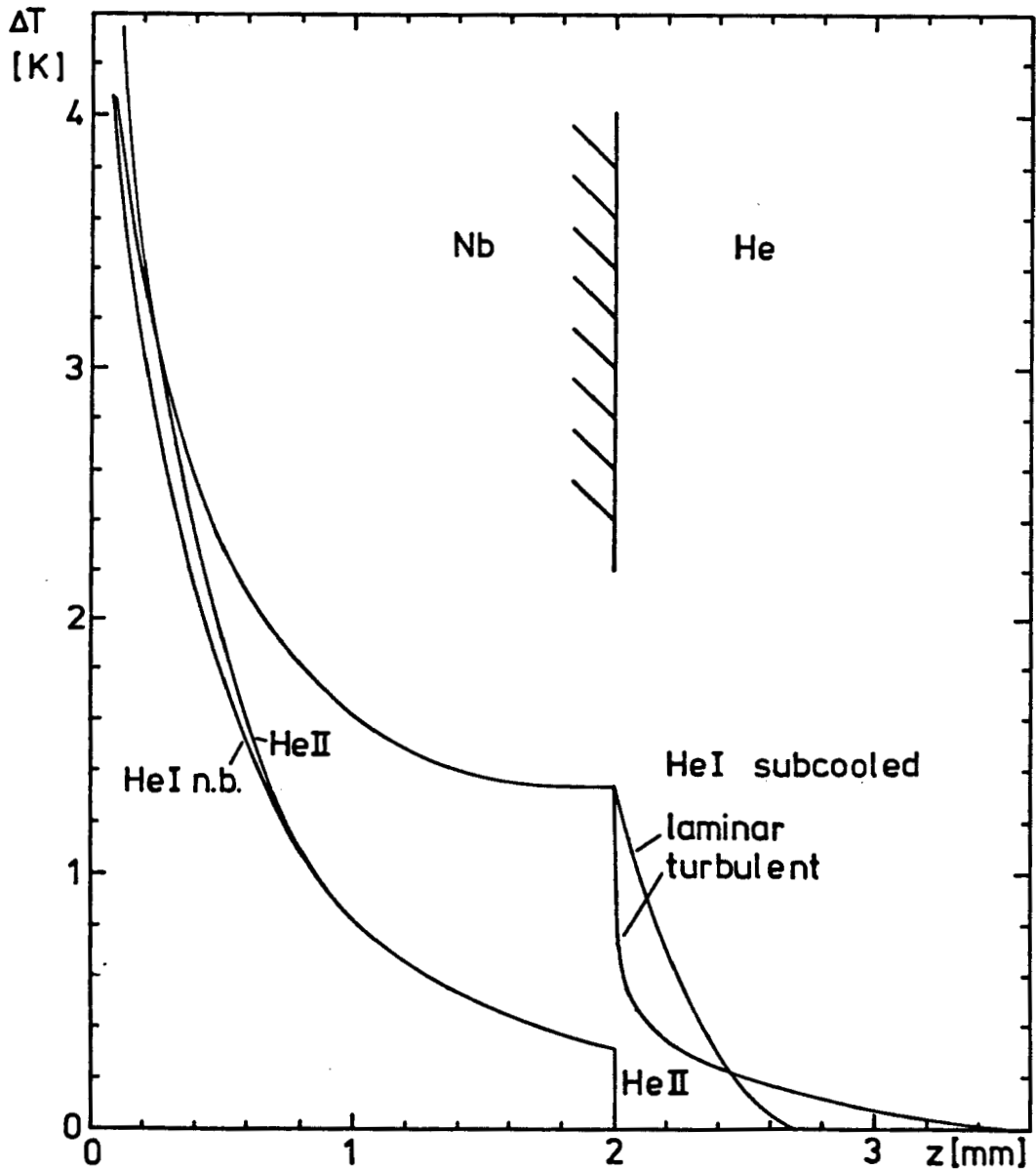


Fig. 1: Temperature profiles (axial) in a Nb wall of typical thermal conductivity (corresp. RRR = 40) due to the RF power loss of a defect (40 mW) for different bath cooling conditions.

in the case of subcooled He I ($T_B = 2.5$ K, pressure 1000mbar) we obtain an enhanced $\Delta T(z = d) \approx 1.34$ K due to the reduced cooling capability.⁸ It is worthwhile to mention that this sensitivity enhancement factor of about 4 is much less than the maximum expected one (≈ 30 , see Fig.6). This is caused by the radial growth of the heated outer wall area in the subcooled case, which leads to a decreased heat current density \dot{Q} .

Compared to the solid the heat transport processes in the liquid Helium are much more complicated.¹⁶ The temperature distributions shown in the Helium region of Fig. 1 are roughly estimated to demonstrate the consequences for temperature mapping. For subcooled He I the heat transfer is dominated by free convection cooling, which can be laminar or turbulent depending on the orientation of the metal surface.^{17,18} Both cases will result in different temperature profiles of the boundary layer, which is expected to be of comparable size as the thermometer resistor.¹⁰ For saturated He I above $\dot{Q} \approx 8$ mW/cm² nucleate boiling starts¹⁹ leading to an undefined temperature fluctuation at the location of the resistors. For He II the enormous thermal conductivity due to the superfluidity causes a sharp drop to the bath temperature just on the metal surface. For all three bath cooling conditions the sensitivity and the accuracy of a temperature mapping system will strongly depend on the efficiency η of the thermometers, which can be defined as the ratio of the measured temperature signal ΔT to the real wall temperature increase. For $\eta \rightarrow 1$, i.e. for thermometers ideally isolated from the Helium bath, quantitative temperature mapping could be done not only in subcooled He I but also in superfluid He II.

There have been some efforts to enhance η of the mostly used Allen Bradley carbon resistors (typ. 100 Ω , 1/8 W)

by grinding off the bakelite insulation or by additional copper tube housings.¹ Also insufficient spring tension and thermal isolation of the resistors against the springs influence η .¹⁰ At CERN the covering of the resistors with silicon rubber led to an increase of η from typically 0.25 to about 0.75⁹ while at Cornell by the use of manganin wires and embedding material for thermal isolation $\eta \leq 0.9$ have been achieved.²⁰ These experiments confirm the assumption that the normally used carbon resistors measure to a large extent the temperature of the surrounding liquid.

At this point the absolute temperature resolution limit of the carbon thermometers shall be mentioned, which corresponds to the fluctuation of the temperature signals without any heat source. With the standard thermometer resistor systems at CERN, DESY and WUPPERTAL typical values of $\Delta T \approx 1-2$ mK can be achieved, which are limited by the AC noise picked up by the wiring between the resistors and the data acquisition systems.

Favourable are multiplexer systems working at Helium bath temperature. Some types of multiplexers show sufficiently low power consumption without any remarkable increase of switching time (for instance Nat.Semi Cond. CD 4051BCJ 21 and Valvo HEF 4051 22). At DESY recently an improved temperature resolution limit of $\Delta T \leq 0.4$ mK has been realized with a new AC (10 kHz) readout technique, which includes a higher dR/dT of the carbon resistors ($\approx 500 \Omega$), cold amplifiers and cold multiplexers.²² At CERN (Cornell) with a single resistor $\Delta T \leq 0.25$ (0.01) mK was reached by using a lock in technique.^{19,20} By technical improvements like these at least a qualitative temperature mapping at very low field levels should be possible in subcooled He I. For a quantitative determination of low residual losses we have to keep in mind that the cooling conditions will change from laminar to turbulent convection above some critical heat current density.¹⁶

As long as we cannot improve the temperature resolution limit and the efficiency of the thermometers drastically, temperature mapping far below quench field level will not be possible under He II bath cooling conditions, i.e. not below $T_B \approx 2.3$ K. For investigation of residual Q-limitations of Nb cavities this restricts the observable local surface resistance R to the well known BCS-value, which scales for frequencies below 3 GHz approximately like $R_{BCS}(2.3 \text{ K}, f) \approx 10^{-8} \Omega \cdot f^2 [\text{GHz}]$ (for $RRR \approx 40$).²³ Moreover for the analysis of field limitations especially for high frequencies the increasing temperature of the Nb surface lead to additional losses due to the exponential growth of $R_{BCS} \propto e^{-18/T} [\text{K}]$, i.e. the higher the RF frequency the lower the achievable field levels, at which temperature mapping in subcooled He I can be done.

In any case the spatial resolution of the scanning thermometer systems for the localisation of defects and electron currents (typically ± 3 mm)⁶ is reduced for increasing field levels by the additional losses due to the BCS surface resistance. The spatial resolution also depends on the thermal conductivity and the thickness of the cavity wall. For the demonstration of these dependencies I will first discuss the results of the model calculations. In Fig. 2 the radial temperature profiles $\Delta T(r)$ at the inner and outer Nb surface in subcooled He I are shown, which are produced by the same defect mentioned already for Fig. 1. Compared are the results for two different thermal conductivities κ (corresponding to $RRR \approx 40$ and 80)²⁴ and RF frequencies (500 MHz and 3 GHz, $H = 150$ Oe, constant $P_D = 40$ mW). At the inner surface (Fig. 2a) the better thermal stabilisation of the defect with increased κ can be seen clearly, corresponding to a higher quench field level of this defect for $RRR 80$.²⁵ Far beside the defect a general heating of the Niobium wall ($T_{iw} - T_{ow} < 5$ mK) against the subcooled bath can be recognized especially for 3 GHz. The temperature response at

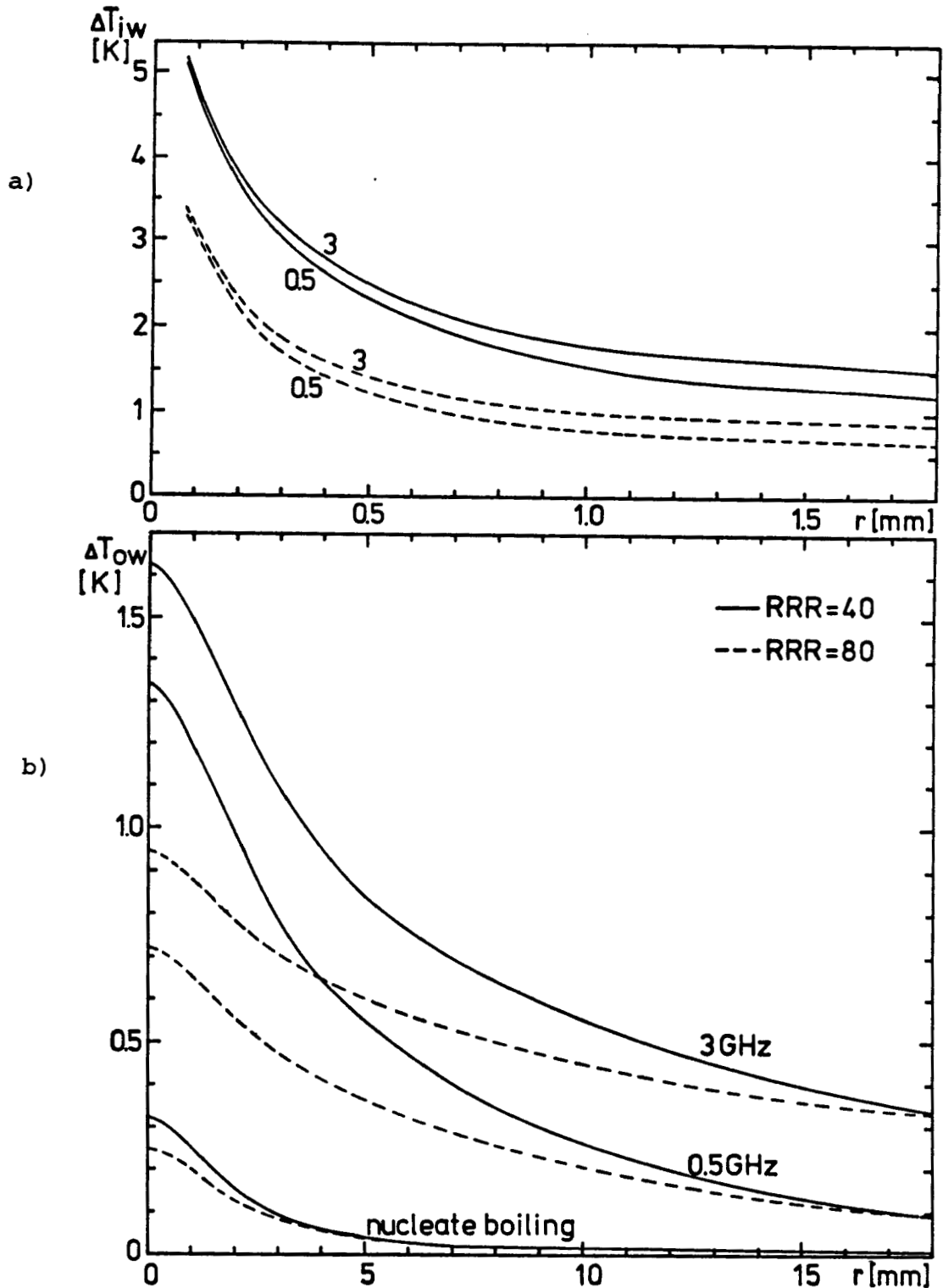


Fig. 2: Temperature profiles (radial) at the inner (a) and outer (b) Nb wall due to the RF power loss of the same defect as in Fig. 1 ($r_D = 150 \mu\text{m}$, $H = 150 \text{ Oe}$, const. $P_D = 40 \text{ mW}$) for different RRR values and RF frequencies under sub-cooled bath conditions ($T_B = 2.5 \text{ K}$). For comparison (3 GHz) also the temperature increase at the outer wall for nucleate boiling He ($T_B = 2.5 \text{ K}$) is given.

the outer wall (Fig. 2b) is lowered and relatively smeared out for increasing κ and f . Further calculations have shown that the ratio of the maximum observable $\Delta T(r = 0)$ to the minimum $\Delta T(r \gg r_D)$ becomes smaller with increasing field level and decreasing defect size.

These considerations have been fully confirmed by recent measurements on Nb cavities of improved thermal conductivity.²⁶ With these cavities up to now the highest accelerating field levels at CERN (500 MHz, up to ~14 MV/m) and Wuppertal (3 GHz, up to ~16.5 MV/m) have been achieved, which may be explained by the better thermal stabilisation or the absence of large defects. In Fig. 3a a temperature map of the 500 MHz cavity is shown. Relatively large areas with increased temperature are visible, and the temperature peaks seem to be not as sharp as those, which are observed usually with cavities of lower κ (Fig. 3b). This flattening of the temperature maps becomes very obvious for the 500 MHz Nb-Cu cavities at CERN.²⁷ The temperature map of the 3 GHz cavity (Fig. 4) exhibits a nearly homogenous heating of the whole surface up to about 900 mK. Here the thermal conductivity only plays a minor role just to allow very high field levels, at which the cavity surface will warm up due to the already substantial BCS losses, which exceed the losses from small defects. This explanation was confirmed by time domain measurements, which has proven that the warm up started at the equator. Therefore, at field levels above 10 MV/m temperature mapping in subcooled He I cannot be applied for 3 GHz Nb cavities.

Nevertheless, at lower frequencies or at lower field levels subcooled He I is up to now the only possible bath cooling condition for a quantitative determination of the heat loss distribution inside a superconducting cavity. For this purpose the correlation between the dissipated power and the temperature increase ΔT measured by a thermometer has to be known.

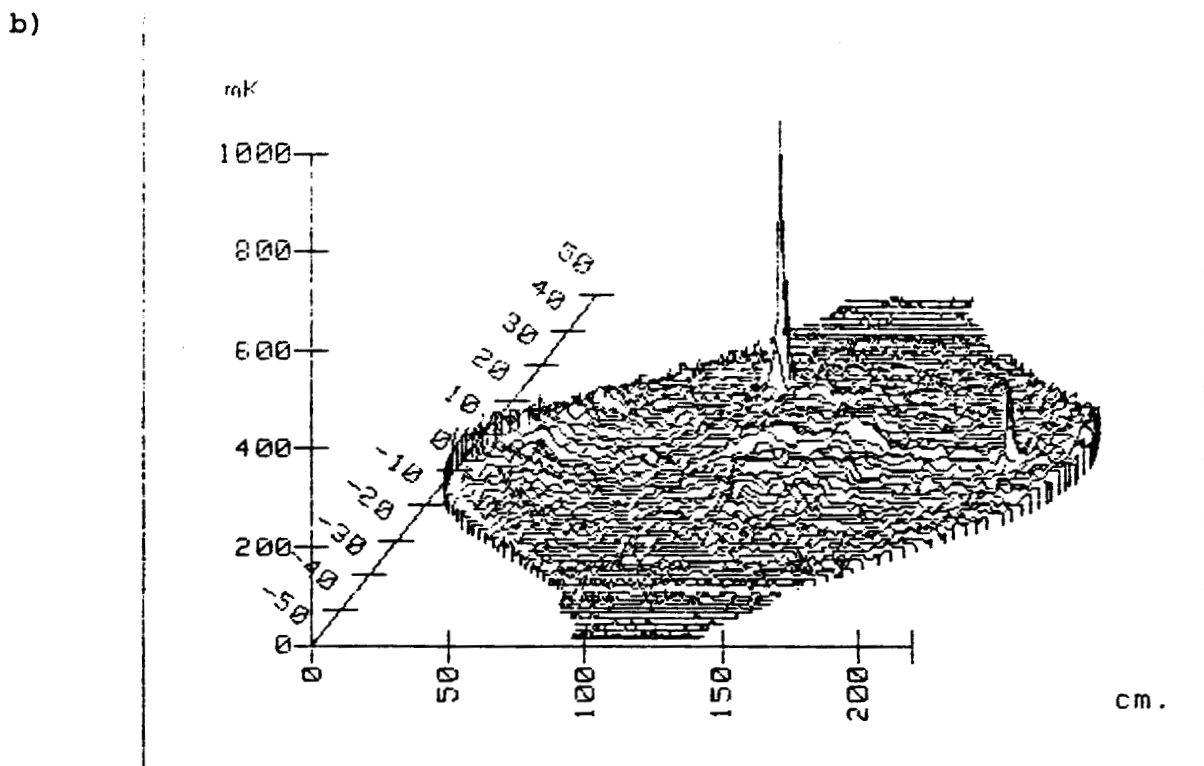
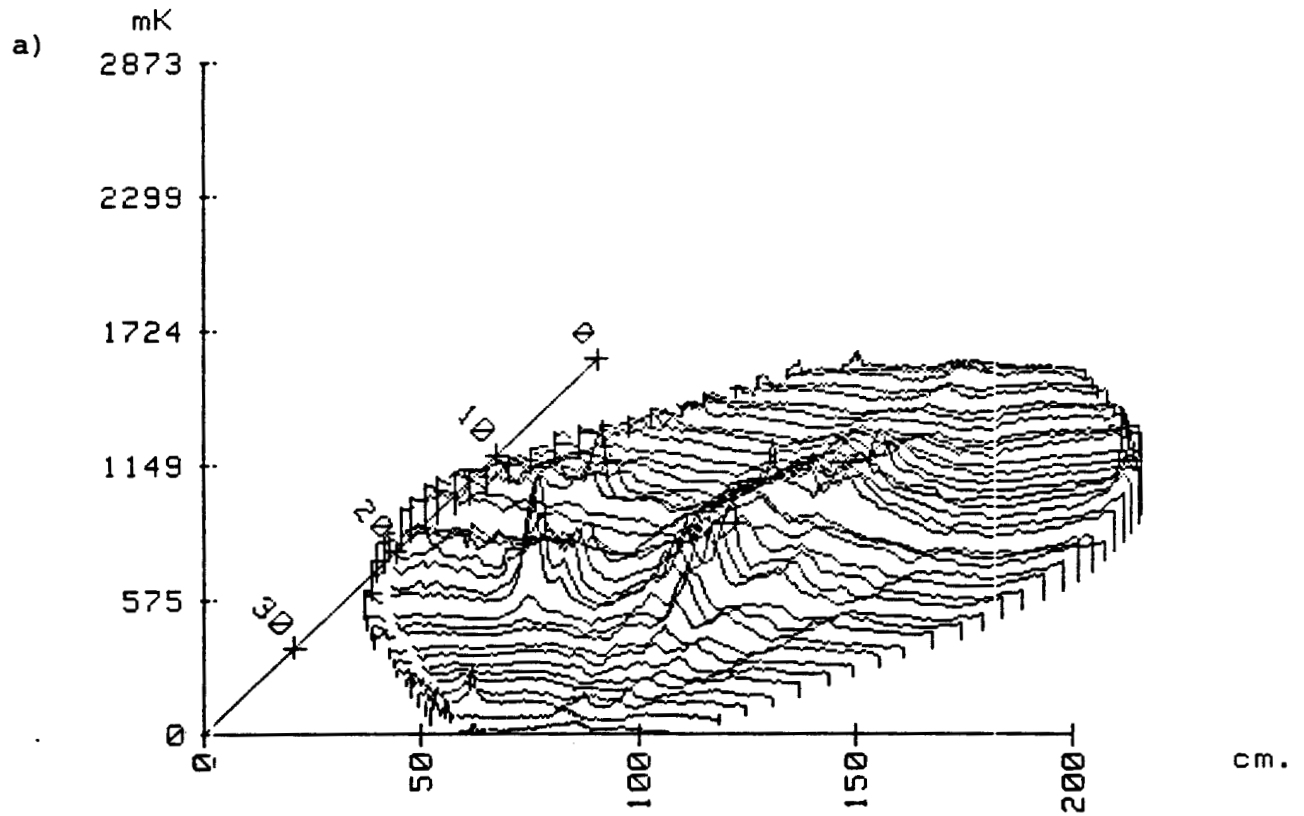


Fig.3: Temperature maps of different Nb cavities (CERN)¹⁹

a) 500 MHz, HERAEUS material (RRR = 110), at $E_{acc} = 8.2$ MV/m

b) 350 MHz, KBI material (RRR = 40), at $E_{acc} = 5.2$ MV/m

In both cavities quenching occurred at the equator without precursors. In addition for b) quenches occurred sometimes at the peak.

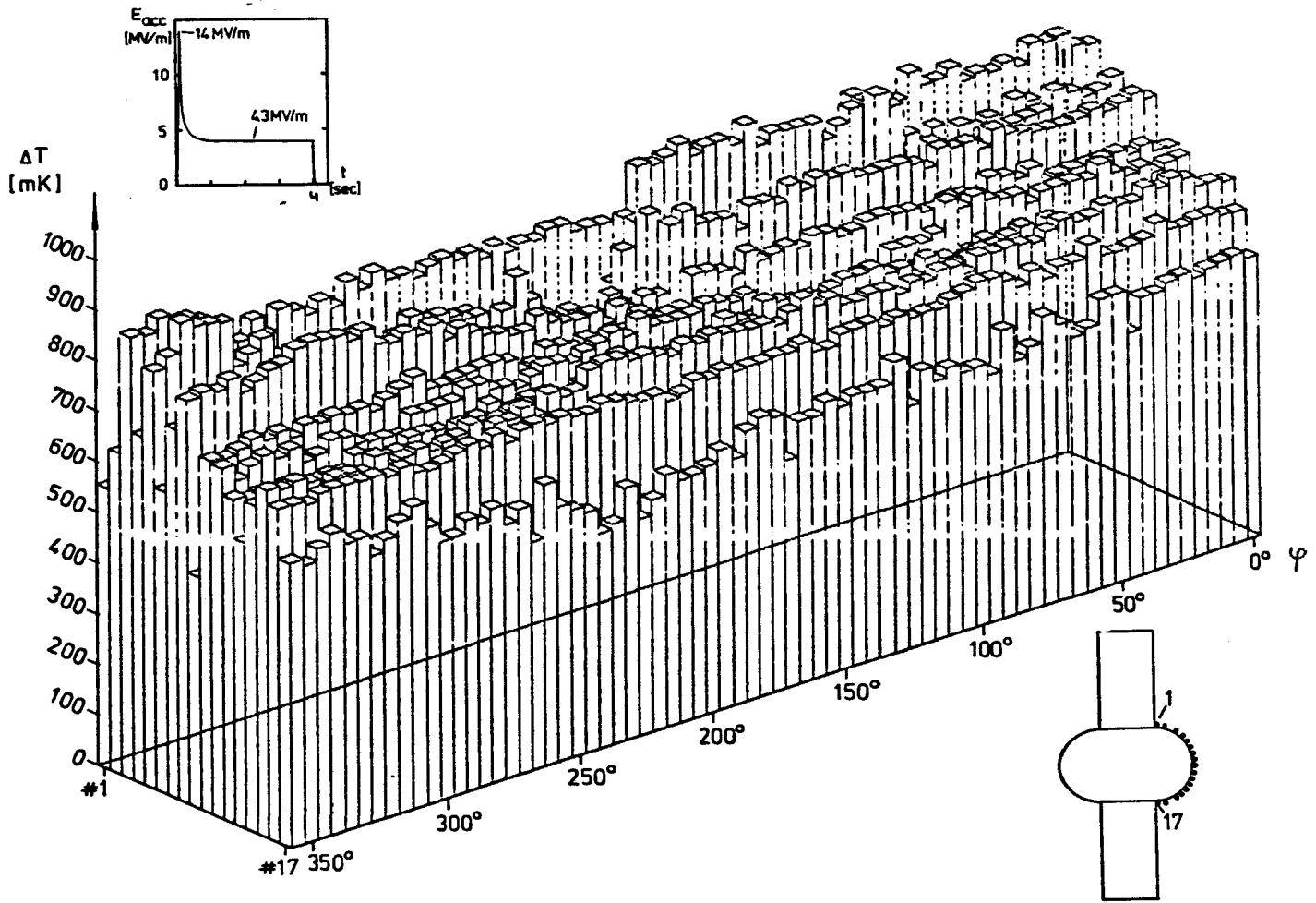


Fig. 4: Temperature map of a 3 GHz Nb cavity of high thermal conductivity (HERAEUS material, $RRR \approx 135$). In this cavity up to now no quench has been observed. The maximum $E_{acc} = 16.5$ MV/m (He II) is limited by a strong field emission of electrons ($\beta = 135$). Homogenous heating occurs due to the high field levels and the exponentially increasing BCS surface resistance, which lead to a strong decoupling of the cavity from 14 to 4.3 MV/m in subcooled He.

As the heat flow depends on the thickness and the thermal conductivity of the wall, it is more convenient to correlate ΔT against the heat current density \dot{Q} at the outer cavity wall. At CERN a special experimental setup (Fig. 5) was used to calibrate the carbon thermometers.^{9,18} By simulating the heat source in a cavity and its cooling mechanism the following result was obtained:

$$\Delta T[\text{mK}] = (33 \pm 3) \dot{Q} \left[\frac{\text{mW}}{\text{cm}^2} \right]^{0.74 \pm 0.05} \text{ for } \dot{Q} \leq 100 \frac{\text{mW}}{\text{cm}^2}, T_B = 2.5 \text{ K}$$

In Fig. 6 the measured data are compared with the theoretically expected wall temperature increase for nucleate boiling and subcooled He I. Since the theoretical slope for natural turbulent (laminar) convection is 0.75 (0.80)^{17,28}, the conclusion was drawn that the cooling is governed by turbulent convection and that the efficiency η of the carbon thermometers is only 0.25. Because of this large influence of the surrounding liquid for real scanning thermometer systems however, it will be more precise to expect at least a varying efficiency $\eta(s)$

$$\Delta T = \alpha \cdot \eta(s) \cdot f(T_B) \dot{Q}^{0.75}$$

where s describes the position of the carbon resistor and $f(T_B)$ takes into account the relative change of the properties of He I with the bath temperature. This will be regarded best by a "in situ" calibration of the scanning thermometer systems, i.e. by measuring ΔT for a known RF power loss distribution in the cavity. At Wuppertal this was realized for the scanning system of the 20 cell accelerating structure (3 GHz) by choosing $T_B = 3.7 \text{ K}$ in order to get dominant BCS-Losses, which have been more than one order of magnitude higher than the residual losses in the calibration measurement. The decreasing of ΔT with increasing

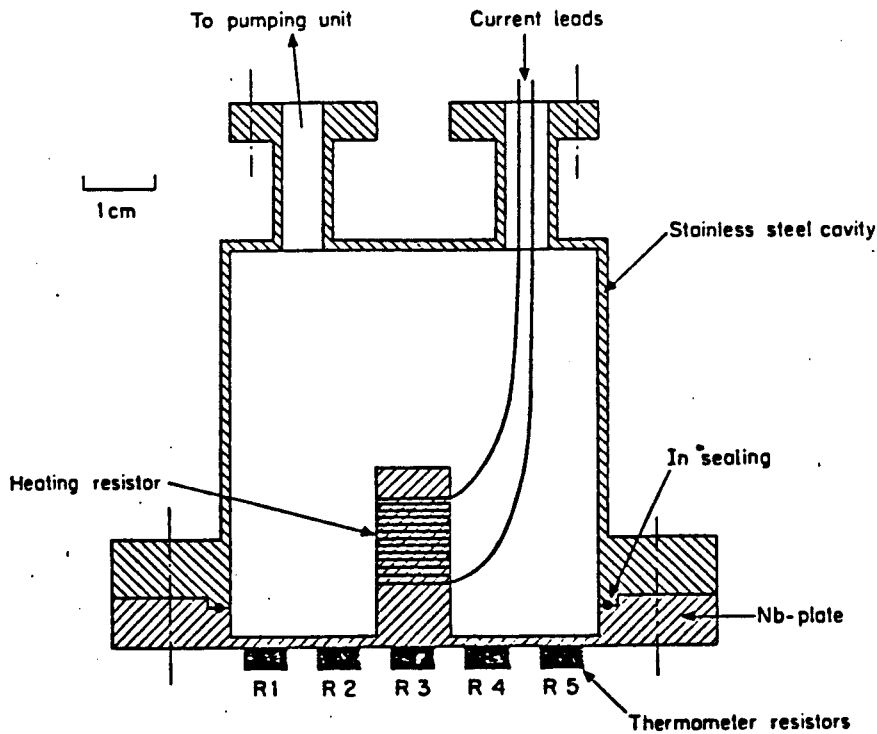


Fig.5: Calibration setup for thermometer resistors¹⁸

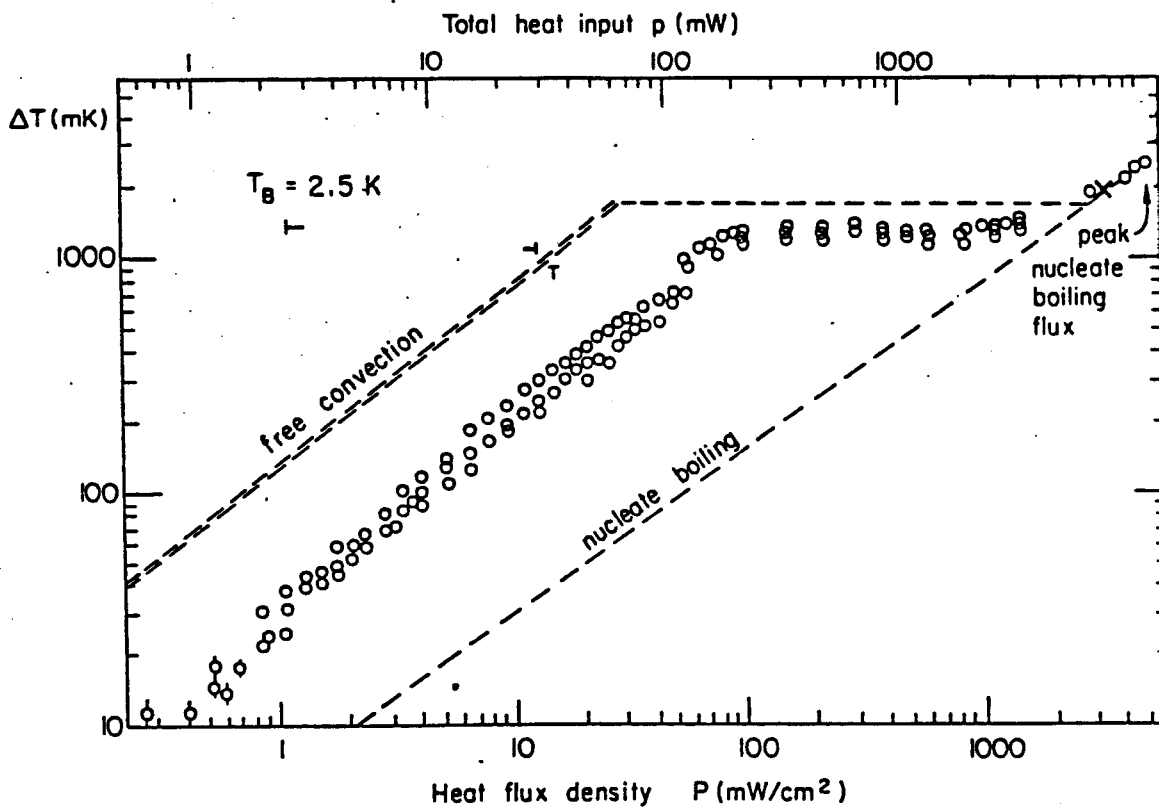


Fig.6: Temperature increase ΔT at R3 (see Fig.5) for different total heat losses and corresp. heat flux densities. The resistor has detected only about 25% of the expected Nb walltemperature increase.¹⁸

T_B can be approximated by the correction function

$$f(T_B) = \frac{\Delta T(T_B)}{\Delta T(2.5K)} = \left(\frac{2.5K}{T_B}\right)^{x(T_B)}$$

where the exponent $x(T_B)$ is only slightly varying with T_B . Measured mean values of x are 1.9 ± 0.5 ⁹ and 1.2 ± 0.1 ¹⁰, from theory^{17,28} we expect $\bar{x} = 1.11$ in the temperature range 2.2 to 4.1 K. The absolute value of the sensitivity α depends on the orientation of the cooling surface¹⁷ and will be higher for regions with poor cooling conditions. By averaging of the measured ΔT over all azimuths and all resistors of relatively same position (concerning RF-field distribution and cooling condition) we have found a strong variation of the product $\alpha \cdot \eta(s)$ between 33 and 400 mK/(mW/cm²)^{0.75} for resistors at the equator and iris respectively.¹⁰ It should be mentioned that we have used the model calculations¹³ to transform \dot{Q} from the inner to the outer cavity wall. In the case of the special calibration device (Fig. 5) this has been proven to be justified.²⁹ Obviously our calibration result means that ΔT -maps can be easily misinterpreted concerning the iris regions. In Fig. 7 this is demonstrated by the comparison of a original measured ΔT -map (Fig. 7a) with the resulting \dot{Q} -map of the 20 cell accelerating structure (Fig. 7b).

Once a scanning thermometer system is calibrated, principally it will be possible to determine the power loss distribution or even the Q_0 of a cavity by temperature mapping. For multicell structures this can be applied to check the field distribution at LHe-temperature. Compared to direct measurements very good agreement was obtained for a 2 cell 500 MHz cavity²⁷ and for the 20 cell 3 GHz structure.³⁰ Moreover a guided detuning for the suppression of a quench in a 4 cell 500 MHz cavity has been reported.²⁷ In many experiments with 350 and 500 MHz cavities the spatial distribution (see Fig. 3b) and the absolute value of

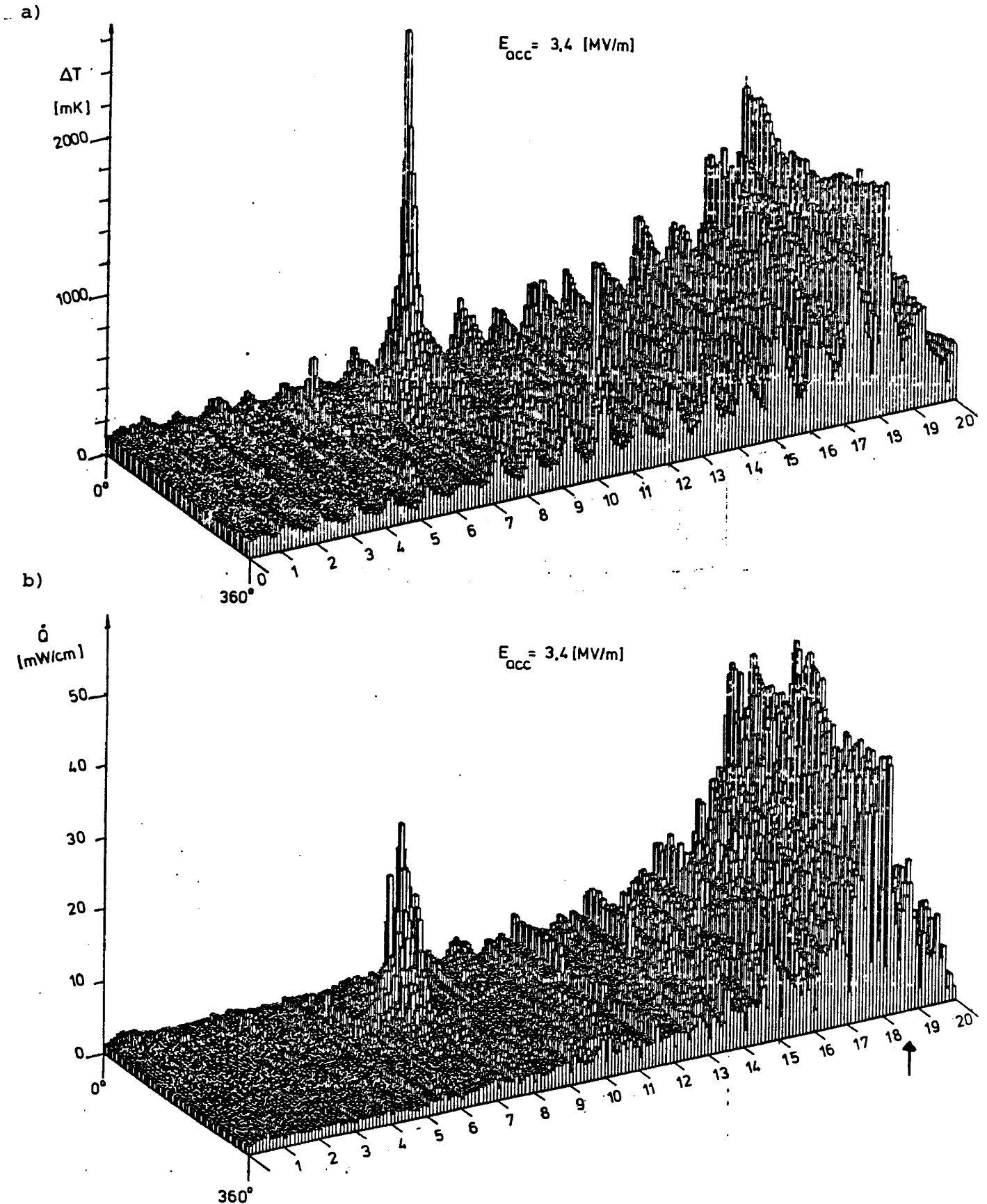


Fig.7: Temperature map (a) and corresponding \dot{Q} -map (b) of the 20 cell accelerating structure (3 GHz).¹⁰ Quenching occurred at a mean field level of $E_{acc} = 4.2$ MV/m in cell no.19 (arrow, 65°). The sharp peak at the iris no.7 is caused by a defect of dielectric nature.

residual losses due to frozen in magnetic flux was determined^{27,31,32}, by which the contribution of the different less known origins of residual losses³³ can be estimated to be typically below a corresponding $R_{res} < 30n\Omega(Q_0 > 10^{10})$.³²

The most interesting application of \dot{Q} -mapping, however, consists in the investigation of the origin of electron loading phenomena and quenching, i.e. in the understanding of the nature of electron emitters and of field limiting defects. For both the knowledge of the linelike or pointlike dissipated power and its dynamic evolution with increasing field level is of fundamental importance. Together with electron trajectory calculations^{6,34,35} pointlike field emitters can be localized.³⁶ From the maximum tolerated defect power just below quench the size of a normal conducting loss area can be concluded, if the thermal conductivity of the wall is known.¹⁵ In Fig. 8 new results of model calculations¹³ for the presently available RRR-values of Nb sheet material are given, showing an almost linear dependence of P_{max} on the defect radius r_D . Moreover from P_{max} , r_D and the local magnetic field the surface resistance R_D of the defect can be estimated. At Cornell in a test series of a 1.5 GHz cavity³⁸ by this method average values of $r_D = (52 \pm 14) \mu m$ and $R_D = (1.8 \pm 1.1) \cdot 10^{-2} \Omega$ at $\bar{H}_{10k} = 330 \pm 110$ Oe have been found for quenching defects³⁷, which proves the normal conducting nature of these defects.

Model calculations with an improved program¹² have shown that small defects can create around itself a normal conducting niobium ring far below quench field level (Fig. 9a). This leads to an additional increase of the dissipated power with increasing field level (Fig. 9b) and should be detectable by an enhanced temperature response

$$\Delta T \propto \dot{Q}^{0.75} \propto H^n \quad n \geq 1.5$$

compared to the normally observed $n = 1.5$.⁶

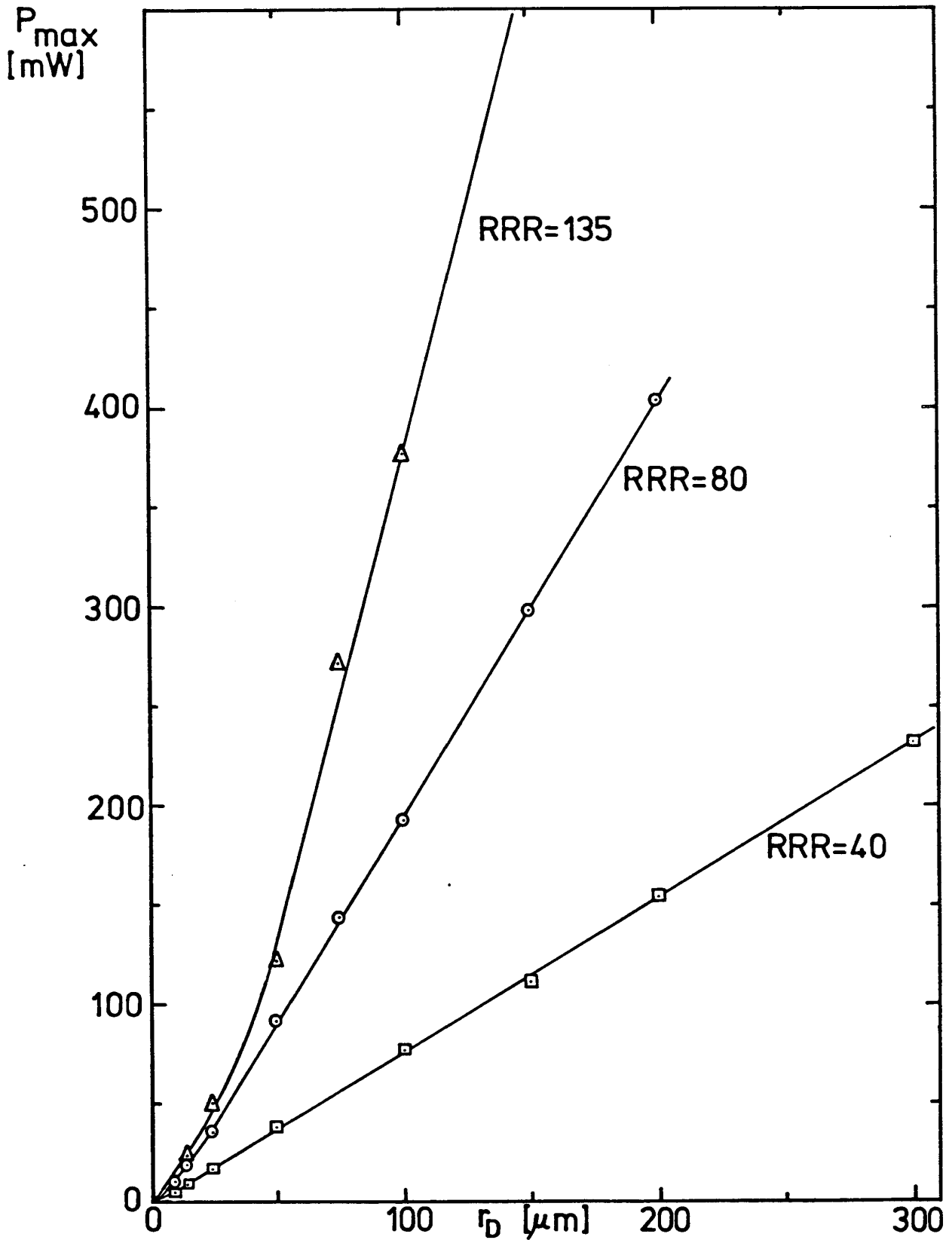
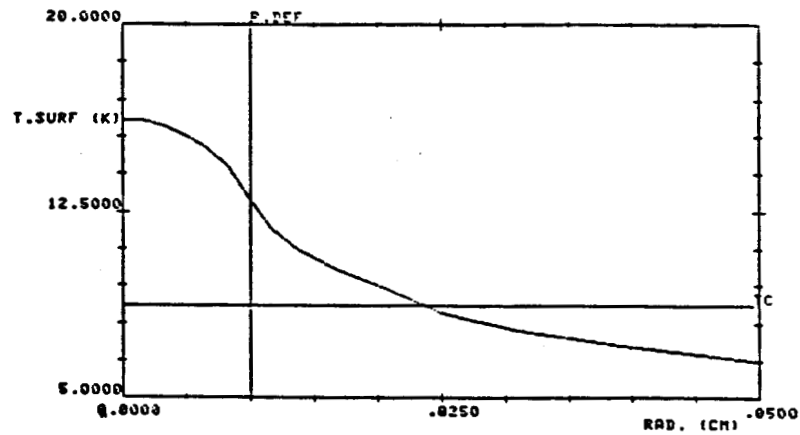


Fig.8: Maximum tolerable power loss of the defect area ($f = 3$ GHz, $T_B = 1.8$ K) versus defect radius for different available RRR values of the Nb wall ($d = 2$ mm).¹³ (compared to Ref.37 the deviation for $r_D > 100 \mu m$ are due to different thermal conductivity functions)

a)



b)

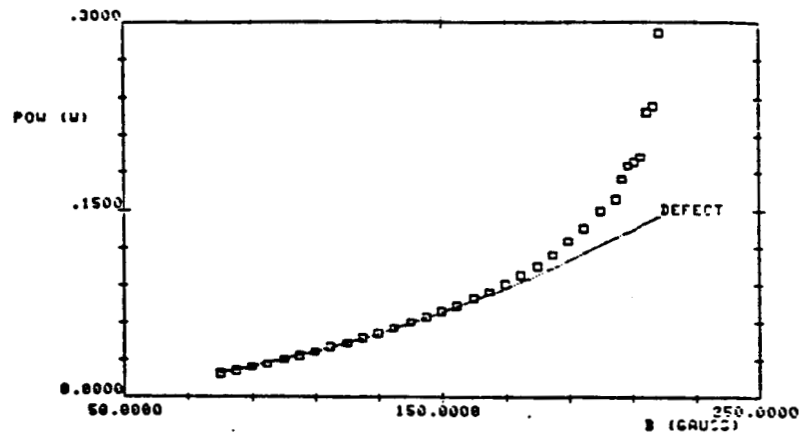


Fig.9: Computer simulated existence of normal conducting rings around a typical defect ($r_D = 100 \mu\text{m}$, $R_D = 8 \cdot 10^{-3} \Omega$)¹²:

- a) Temperature profile (radial) at the inner cavity wall
($H = 215 \text{ Oe}$, $f = 500 \text{ MHz}$, $T_B = 2.5 \text{ K}$ subcooled)
- b) Enhanced power loss at high field levels due to the ring

A special effect of a suddenly enhanced temperature response appears, if small regions of the superconducting surface are nearly thermally isolated, which can be easily simulated by model calculations. These have shown¹² that at a certain field level H_s the bad cooling condition lead to a thermally induced phase transition to the normal conducting state. Depending on the size of this area quenching must not occur simultaneously. In this case only a small drop of the cavity Q_0 results, which disappears at a lower recovery field level $H_r < H_s$. So this kind of defect can be switched on and off at certain field levels. Such Q-switches have been observed for a lot of cavities, rather accentuated for small cavities, i.e. high frequencies.³⁹ In Nb-Cu cavities²⁷ and Nb₃Sn cavities⁴⁰ they often limits the achievable Q_0 at high field levels. Principally a Q-switching behaviour can be caused also by a magnetically induced phase transition due to a reduced critical field of a weak spot.⁴¹ Recently such a weak spot has been identified in a 20 GHz Nb₃Sn cavity⁴² by its quadratic dependence on bath temperature $H_s(T) = H_s(0) (1 - (\frac{T}{T_c})^2)$, giving $T_c \approx 9.9$ K and $H_s(0) \approx 26$ Oe (if the weak spot is located in maximum H field region).

Enhanced temperature responses of defects up to $n = 3$ have been measured in a series of experiments with a 500 MHz cavity⁶, sometimes associated with Q switches. Electron loading phenomena show up even a much stronger increase of wall temperature. From all the above we can conclude, that it is not possible to scale temperature maps in advance for a prediction of the next quench field level after the guided removal of the old defects.

III. Classification of defects

In a wide sense defects are all those irregularities of a real cavity surface, which lead to additional RF power losses compared to that of an ideal superconducting surface. At first we can separate defects, which limit up to now only the achievable Q_0 of cavities due to residual losses³³ like frozen in magnetic flux cores, surface oxides, gas adsorbates and all particles of foreign material in the submicron range. Some of these may also influence electron loading phenomena, which will be reported in other talks.^{36,43} I shall concentrate on field limiting defects leading to quenching. In former times these have been called generally weak spots⁴¹, knowing that there are a lot of possible reasons for the local heating of the cavity surface as for instance large bad spots of enhanced residual losses or of reduced critical magnetic field and heat sources due to the impact of high intensity and high energy electrons. Since systematic temperature mapping allows not only the localisation of quenching areas but also the distinction of the different reasons for quenching, we have learned somewhat more about the nature of the corresponding defects by the subsequent inspection of the cavity surface.

For the inspection of the inner cavity surface generally endoscope or telescope systems are used, by which defects above a minimum size of about 50 μm can be observed. This is already a magnification of about 5 compared to the resolution limit of the human eye. Much higher magnifications can be reached of course with scanning electron microscopes (SEM), which in addition often allow elemental analysis down to Neon ($Z = 10$). The inspection of defects with a SEM however requires the destruction of the cavity, which has been carried out at CERN for some 3 GHz cavities. Alternatively for low frequencies special SEMs can be developed by using the cavity as its own vacuum chamber. At CERN such a SEM (without elemental

analysis) has been built for 500 MHz cavities.⁴⁴ If the defect can be found by these methods, at least some scraped material may be analysed.

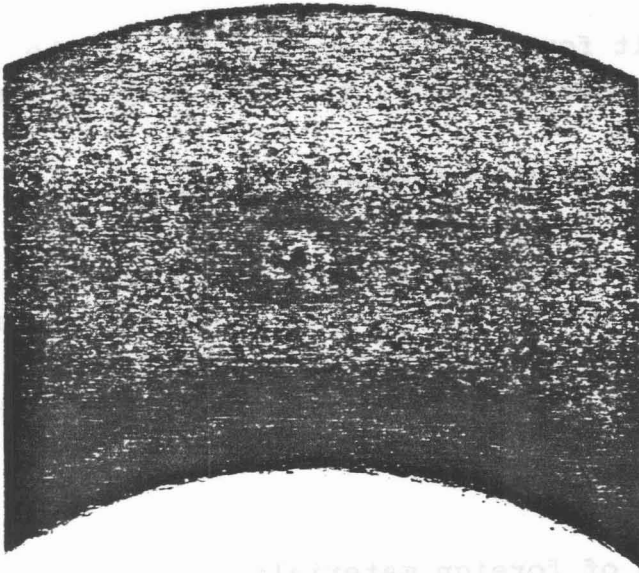
During the last years systematic temperature mapping and subsequent inspection of the quenching area has become a routine work at many laboratories, sometimes including the chemical analysis of defects. A lot of Niobium cavities have been investigated by these means up to now. In these experiments various kinds of field limiting surface defects have been identified, which we can divide into two main classes:

- A) Regions of foreign materials
- B) Geometrical irregularities of the Nb surface.

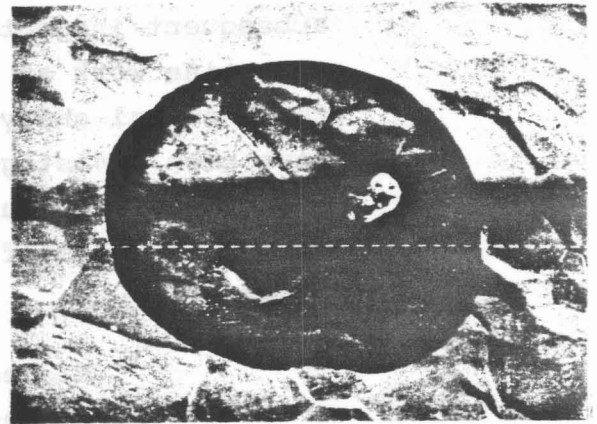
It is convenient to subdivide both classes into several categories due to their special visual appearance:

- A 1) Central spot with dark looking halo^{19,45,46} (Fig. 10a)
The diameter of the halo often exceeds 1 mm. Following elements ($Z > 10$) have been found: Cu, Fe, Mg, Zn, Pb, ...
It seems that the halo arises due to the RF field, sometimes accompanied by a strong permanent degradation of Q_0 and E_{acc} . In Fig. 11 the corresponding change of the temperature map of such a halo is demonstrated.
- A 2) Small dark spots²⁷, consisting of Cl, K, Ca, Al, Pb, S, Si,
They are often localized in the near of couplers and joints
- A 3) Drying stains^{27,45} (Fig. 10b), consisting of K, Cl, P, Ca, Na ...
They are most likely produced by wet surface treatments and are presumed to be of dielectric nature.
- A 4) Small Crystals⁴⁵ (Fig. 10c), consisting of S, Ca, Cl, K ...

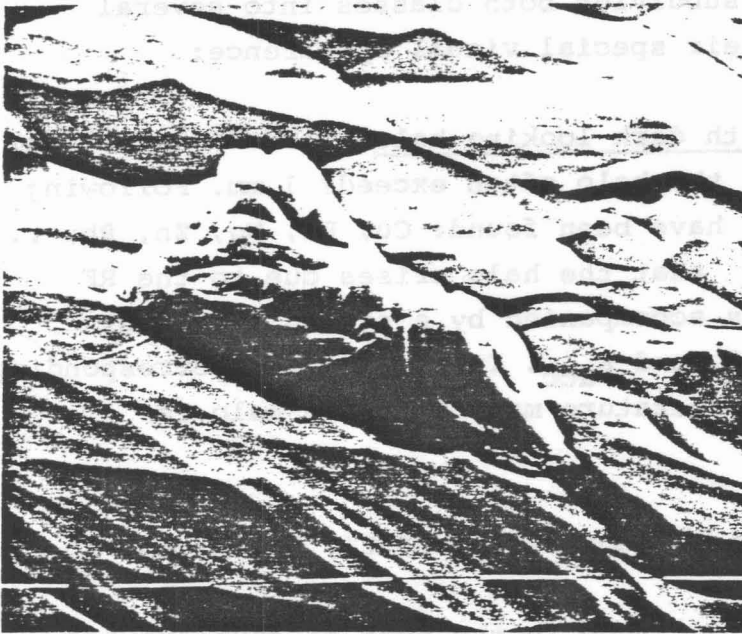
a)



b)



c)



d)

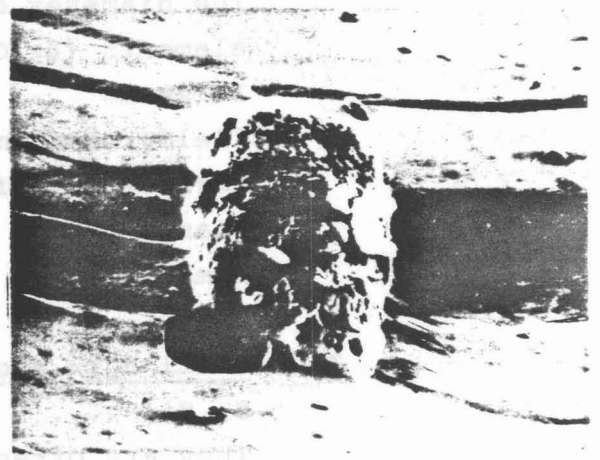


Fig.10: Examples for defects consisting of foreign materials⁴⁵

 E_{acc}^{max}

- | | |
|---|-----------|
| a) Central spot with dark looking halo (\varnothing 4 mm), light obs. | 2.9 MV/m |
| b) Drying stain (\varnothing 440 μ m; K, Cl, P) with small crystal, H reg. | 3.4 MV/m |
| c) Small crystal (\varnothing 50 μ m; S, Ca, Cl, K) two in H field region | 10.7 MV/m |
| d) Metallic inclusion ($\approx \varnothing$ 360 μ m; W) at TIG weld | 4.5 MV/m |

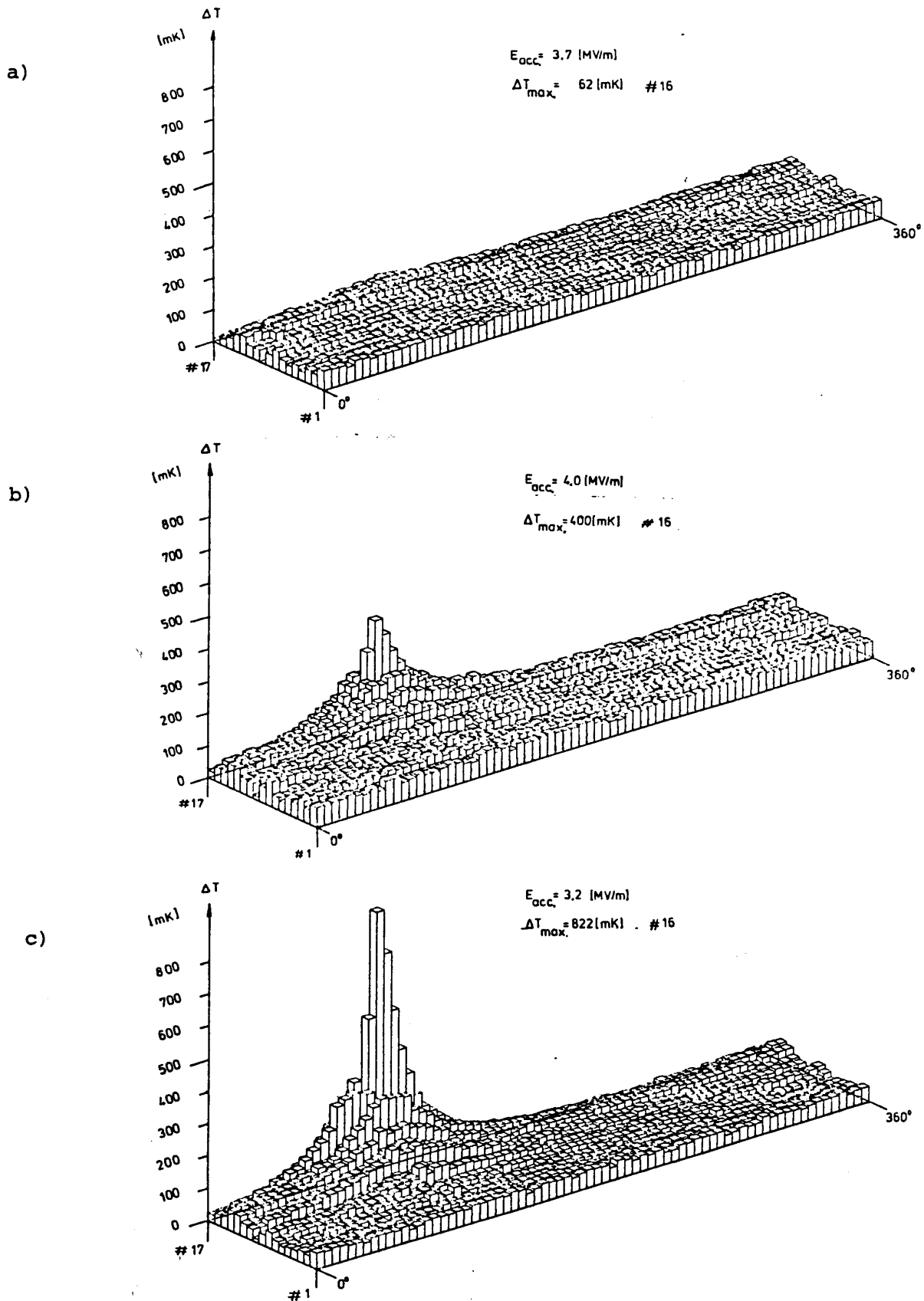


Fig.11: Changing of the temperature maps of a 3GHz Nb cavity^{4,6} due to the arising of a "halo" defect a) before first quenching b) after the first quenches c) after about 1h of RF processing

- A 5) Metallic inclusions ^{27,45,47} (Fig. 10d), consisting of W, Ta, Fe, Pb, Zn, Al
They exist already in the Nb Sheet material or will be produced during the fabrication of the cavity.
- B 1) Welding beads ⁴⁵⁻⁴⁷ (Fig. 12a)
They mostly cause a switching behaviour before quenching and can easily be feeled with the fingertips.
- B 2) Holes with sharp edges ^{27,45} (Fig. 12b)
They have been observed only in TIG welds.
- B 3) Whiskers and scratches ^{45,46} (Fig. 12c)
They appear after grinding with burrs or other tools.
- B 4) Microfissures ^{47,48} (Fig. 12d)
They are often associated with welds.
- B 5) Porosity of welding ⁴⁷
This occurs especially in the overlap region of two welds.

Surely this list of categories may be enlarged by some others, since I have summarized only the accessible ones. However, there is an important difference between both classes. While class A categories will cause different kinds of losses due to their electrical conductivity, as for instance dielectric losses or normal conducting metal losses, B categories have to become at first normal conducting in the RF field due to their poor thermal contact to the bulk material. Most of these defects are of rather trivial nature and have given valuable hints for the improvement of the fabrication and preparation of the Nb cavities, as for instance grinding of the weldings, looking for discoloured spots after anodizing of the cavity and final rinsing with demineralized, dustfree water. A straight forward consequence to get rid of most of these defects is the tumbling method developed at DESY.⁴⁹ In Fig.13

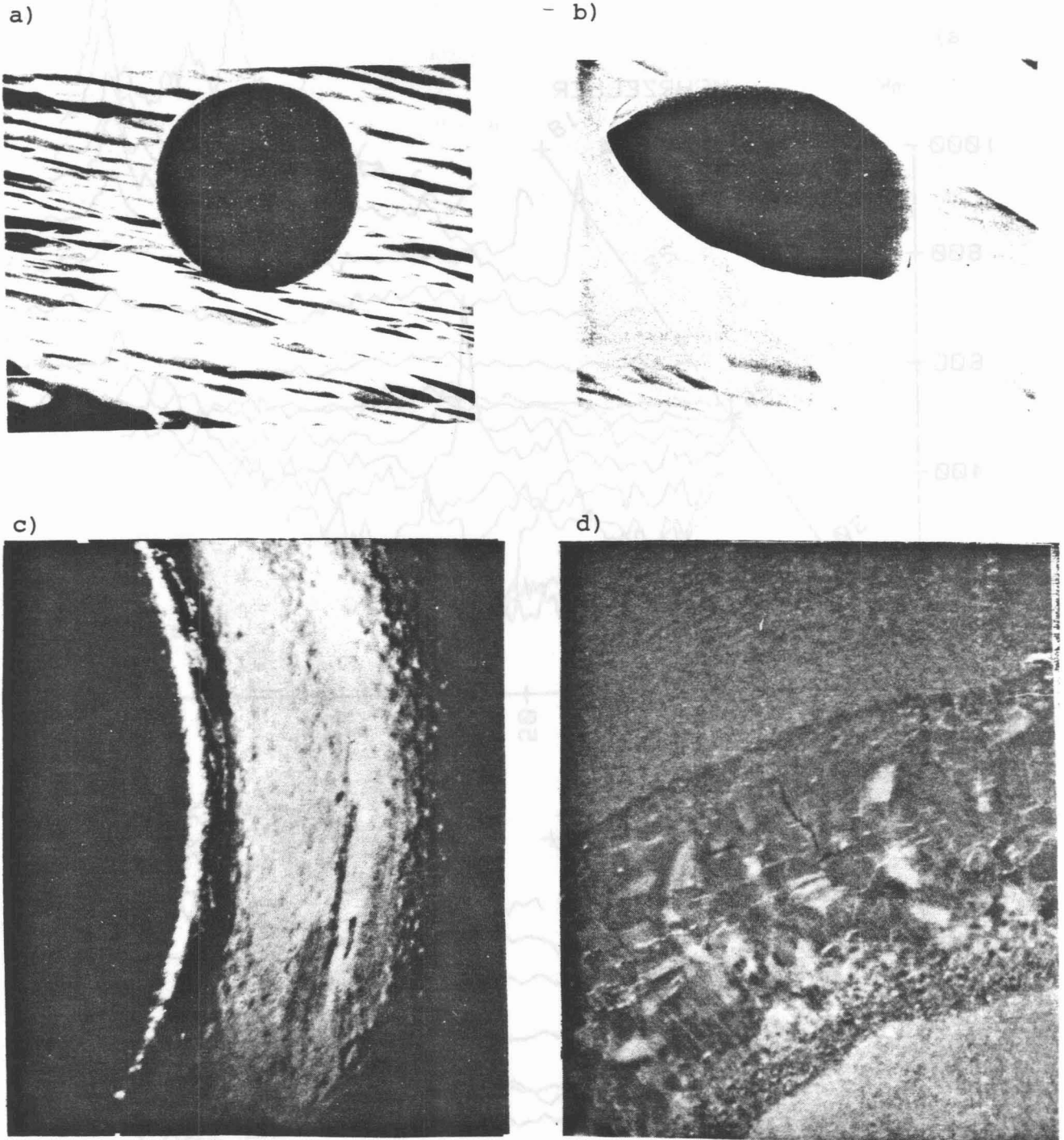


Fig.12: Examples for defects due to geometrical irregularities E_{acc}^{max}

a) Nb-sphere ⁴⁵ (\varnothing 80 μ m) causing Q-switching, H field reg.	6.8 MV/m
b) Hole with sharp edges ⁴⁵ (\varnothing 130 μ m) 3 of them in TIG weld	3.7 MV/m
c) Scratches ⁴⁶ (\approx 0.1 x 3 mm) due to grinding	7.3 MV/m
d) Microfissures ⁴⁸ (\approx 20 x 500 μ m) in TIG weld	3.2 MV/m

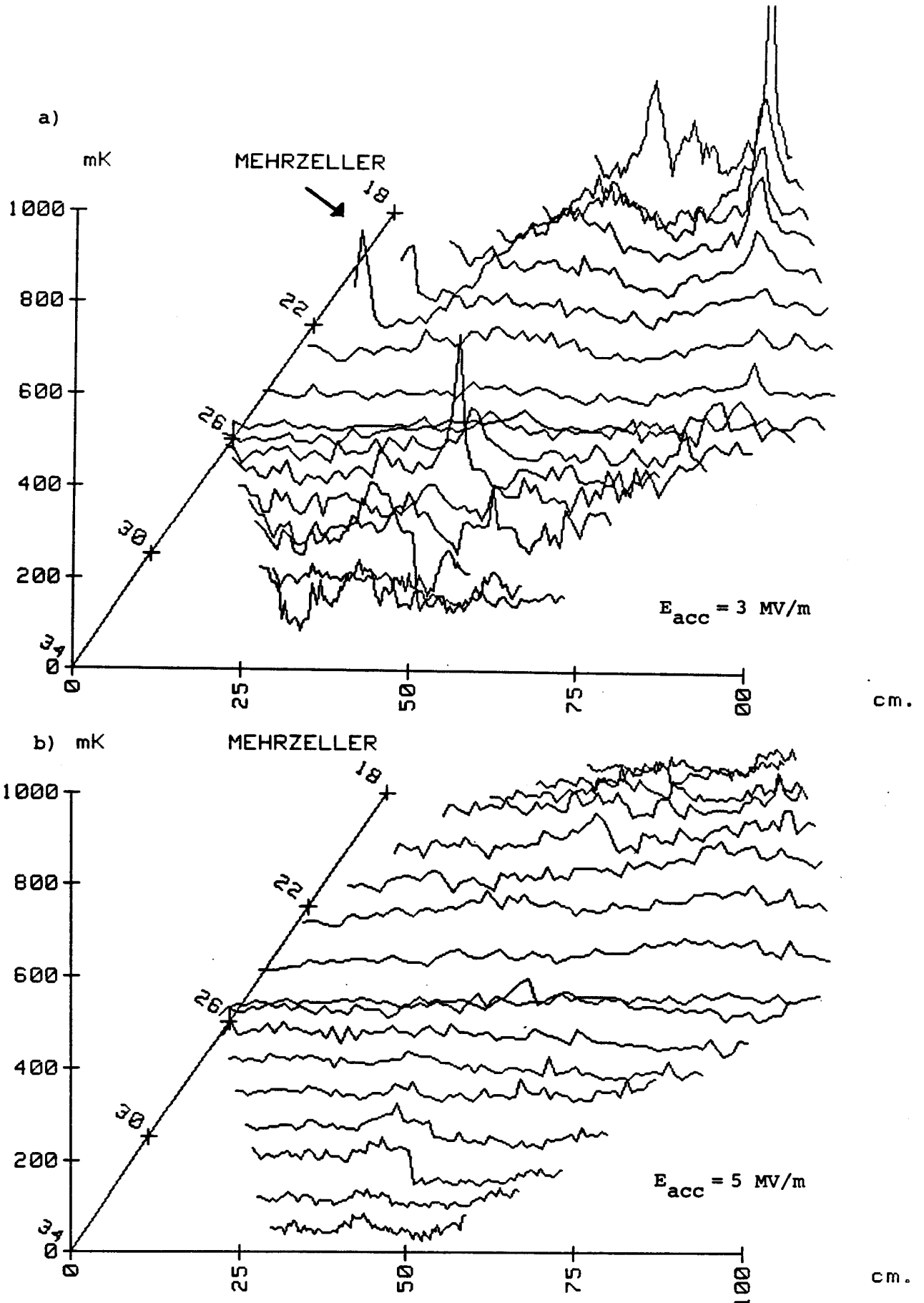


Fig.13: Temperature maps of the second cell of a 9 cell cavity (DESY) before (a) and after (b) tumbling.⁴⁹ The quench area of (a) is indicated.

this is demonstrated by the comparison of temperature maps of the second cell of a 9 cell structure (1 GHz) before and after tumbling. Although a correlation between special categories and the corresponding quench field levels cannot be recognized, the more recent experiments have shown that defects at the welding seams (especially B 4 and B 5) are the most severe ones for field levels above 5 MV/m. Moreover it must be mentioned, that at these quench field levels often defects cannot be found anymore without optical magnification.

Hidden defects at high quench field levels H_q are not really astonishing, if we remember the model calculations. In Fig. 14 for the available RRR values the dependence of H_q on the size r_D and the surface resistance R_D of a normal conducting defect is shown. For a given thickness ($d = 2$ mm) and thermal conductivity ($\kappa(4.2 \text{ K}) \approx \text{RRR}/4 \text{ W/mK}$) of the Nb wall r_D will decrease about quadratically with increasing H_q . As $R_D \propto \sqrt{f}/\sigma$ (normal skin effect assumed) for a given H_q the defects will be even smaller at low frequencies, which is the reason for choosing the product $r_D \cdot R_D$ as axis in Fig. 14. In the case of category B defects (Nb !) because of $\sigma \propto \text{RRR}$ we can conclude further $H_q \propto (\text{RRR})^{1/4}$, which favours higher RRR material in addition to the better thermal stabilisation of such defects.

Recent experiments with cavities of improved thermal conductivity²⁶ show indeed no quenching due to defects up to field levels of about $H_p = 500 \text{ Oe}$ (corresponding $E_{\text{acc}} = 14 \text{ MV/m}$, 500 MHz) and $H_p = 700 \text{ Oe}$ ($E_{\text{acc}} = 16.5 \text{ MV/m}$, 3 GHz), but in the 500 MHz cavities sometimes electron induced quenches occur at the equator due to multipacting.³⁶ At the corresponding electric peak field levels of $E_p = 30 - 40 \text{ MV/m}$ mostly strong field emission loading limits the achievable field level, which can be influenced by He-ion sputtering. Moreover by this

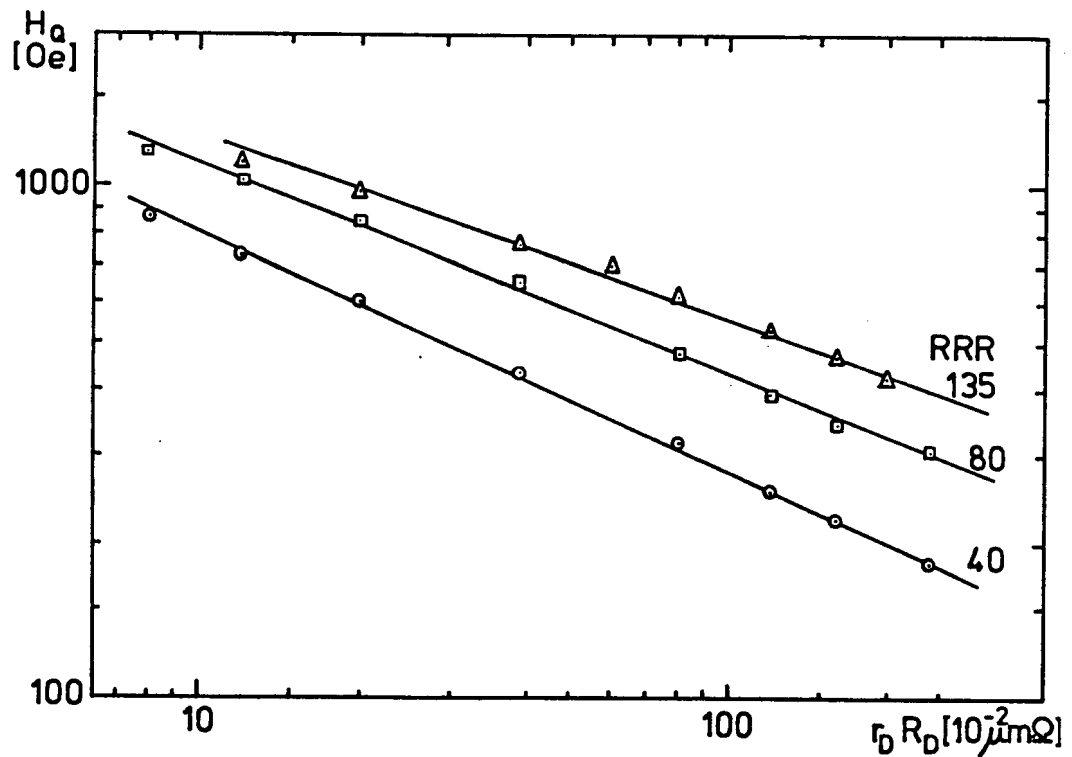


Fig.14: Quench field level H_Q versus the product radius times surface resistance of a defect for the same conditions as in Fig.8

method (or even by high field RF processing) sometimes new defects have been created (see Fig. 15) or lossy spots disappeared.^{19,46} It has been assumed often that dust particles, which may be emitters of electrons, can be evaporated at high electric field levels. For the investigation of these phenomena, which change during the operation of a cavity, beside systematic temperature mapping other diagnostic techniques have to be applied again, especially the scanning X-ray detectors.¹

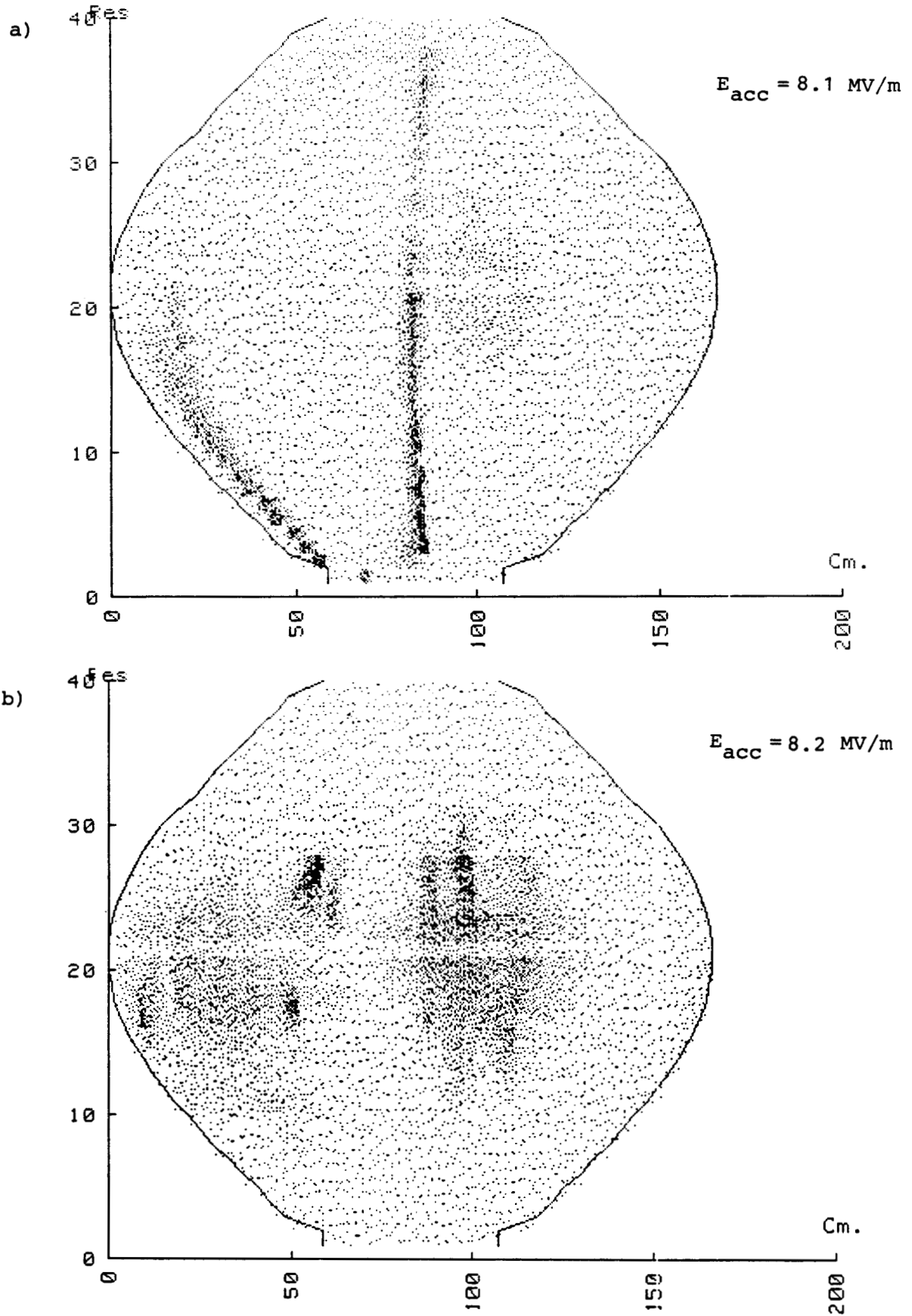


Fig.15: Temperature map of a 500 MHz Nb cavity (HERAEUS mat. RRR=110) before (a) and after (b) He-ion sputtering (6h)

IV. Concluding remarks

Twelve years ago P.B.Wilson ⁵⁰ suggested a statistical model for magnetic field breakdown. From the enhanced probability of finding defects with increasing cavity surface he concluded that at lower frequencies lower breakdown fields have to be expected. This will be surely true on the average, if we don't localize and remove the field limiting defects. The guided repair of cavities, i.e. the application of systematic temperature mapping and other locally sensitive diagnostic techniques, has proven to be one of the means to achieve roughly the same field levels at all frequencies. It is hoped that temperature mapping remains a useful tool in the understanding of field emission loading, which is the next limitation to be overcome.

Acknowledgements

I am very thankful to H.Piel, H.Lengeler and W.Weingarten for the valuable hints and discussions on these subjects during the last months. I am especially grateful to H.Elias, D.Huppelsberg and A.Matheisen for the help during course of preparing this talk. Many thanks are due to D.Proch, K.W.Shepard, H.Padamsee, P.Kneisel and J.Tückmantel for their contributions.

References

1. H.Piel, Proc. of the Workshop on RF Superconductivity, Karlsruhe, KfK-3019,85(1980)
2. Ph.Bernard et al., Proc. of the 11th Int.Conf. on High Energy Acc., Geneva, p.878(1980)
3. M.Tigner, IEEE Trans.Nucl.Sci. NS-30, 3309 (1983)
4. H.Piel, Proc. of the 12th Int.Conf. on High Energy Acc., Fermilab, p.571(1983)
5. H. Piel, Proc. of the Linear Acc.Conf., Seeheim/Darmstadt (1984)
6. Ph.Bernard et al., Nucl.Instr.Meth.190,257 (1981)
7. K.W.Shepard et al., IEEE Trans.Nucl.Sci NS-24, 1147(1977)
8. R.Romyn, H.Piel, CERN/EF/RF 80-3(1980)
9. R.Romyn, W.Weingarten, H.Piel, IEEE Trans.Magn.MAG-19, 1318(1983)
10. D.Huppelsberg, piv. comm.
11. H.Padamsee, IEEE Trans.Magn. MAG-19,1322(1983)
12. J.Tückmantel, CERN/EF/RF 84-6 (1984)
13. H.Elias, priv. comm.
14. K.Krafft, Cornell University, thesis (1983)
15. H.Padamsee, CERN/EF/RF 82-5(1982)
16. H.Padamsee, Proc. of the Workshop on RF Superconductivity, Karlsruhe KfK-3019,145(1980)
17. W.H. McAdams, Heat transmission, McGraw Hill, New York (1954)
18. R.Romyn, W.Weingarten, CERN/EF/RF 81-4(1981)
19. W.Weingarten, priv. comm.
20. P.Kneisel, priv. comm.
21. R.Romyn, priv. comm.
22. J.Peters, priv. comm.
23. U.Klein, University of Wuppertal, thesis, WU DI 81-2 (1981)
24. G.Meuser, priv. comm.
25. H.Padamsee, this workshop
26. W.Weingarten, G.Müller, H.Piel, contribution to the Appl. Supercond. Conf., San Diego (1984)
27. C.Benvenuti et al., CERN/EF/RF 84-3(1984)
28. R.D. McCarty, NBS Technical Note 631(1972)

29. H.Padamsee, CERN/EF/RF/ 82-4(1982)
30. T.Grundey, U.Keiper, priv. comm.
31. Ph.Bernard et al., Nucl.Instr.Meth. 206, 47(1983)
32. Ph.Bernard et al., CERN/EF/RF 82-9(1982)
33. J.Halbritter, this workshop
34. C.Lyneis, Proc. of the Workshop on RF Superconductivity, Karlsruhe, KfF-3019,119(1980)
35. U.Klein, D.Proch, Proc. of the Conf. on Future Possibilities for Electron Accelerators, Charlottesville (1979)
36. W.Weingarten, this workshop
37. H.Padamsee, Cornell University SRF 840403(1984)
38. P.Kneisel, Cornell University SRF 831203(1983)
39. G.Müller, University of Wuppertal, thesis, WUB-DI 83-1(1983)
40. G.Arnolds-Mayer, this workshop
41. C.Lyneis et al., IEEE.Trans.Magn. MAG-11, 417(1975)
42. N.Klein, priv. comm.
43. R.V.Latham, this workshop
44. A.G.Mathewson, A.Grillot, CERN-ISR-VA/81-34(1981)
45. H.Padamsee, J.Tückmantel, W.Weingarten, IEEE Trans.Magn. MAG19,1308(1983)
46. A.Matheisen, priv. comm.
47. K.W.Shepard, priv. comm.
48. A. Scharding, priv. comm.
49. D.Proch, priv. comm.
50. P.B.Wilson, Proc. of the Conf. on Proton Linear Acc., Los Alamos (1972)